HOFFMAN, D. M. & SUH, S. (1994). Personal communication.
KIRKPATRICK, S., GELATT, C. D. JR & VECCHI, M. P. (1983). *Science*, **220**, 671–680
KRAUSE, K. L. (1994). Personal communication.
METROPOLIS, N., ROSENBLUTH, M., ROSENBLUTH, A., TELLER, A. & TELLER, E. (1953). *J. Chem. Phys.* **21**, 1087–1092.
MILLER, R., DETITTA, G. T., JONES, R., LANGS, D. A., WEEKS, C. M. & HAUPTMAN, H. A. (1993). *Science*, **259**, 1430–1433.

PRESS, W. H., TEUKOLSKY, S. A., VETTERLING, W. T. & FLANNERY, B. P. (1992). *Numerical Recipes: the Art of Scientific Computing*, pp. 436–448. Cambridge Univ. Press.
RATHORE, R., BOSCH, E. & KOCHI, J. K. (1994). *J. Chem. Soc. Perkin Trans.* 2, pp. 1157–1166.
SEMENOVSKAYA, S. V., KHACHATURYAN, K. A. & KHACHATURYAN, A. G. (1985). *Acta Cryst.* A41, 268.
SERRA, D. L. & HWU, S.-J. (1992). *J. Solid State Chem.* **101**, 32–40.

Structure Determination by Electron Crystallography Using Both Maximum-Entropy and Simulation Approaches

BY I. G. VOIGT-MARTIN, D. H. YAN AND A. YAKIMANSKY*

Institut für Physikalische Chemie der Universität Mainz, Jakob Welder Weg 11, 55099 Mainz, Germany

D. SCHOLLMEYER

Institut für Organische Chemie der Universität Mainz, Jakob Welder Weg 11, 55099 Mainz, Germany

C. J. GILMORE

Department of Chemistry, University of Glasgow, Glasgow G12 8QQ, Scotland

AND G. BRICOGNE

*MRC Laboratory of Molecular Biology, Hills Road, Cambridge CB2 2QH, England,
and LURE, Bâtiment 209D, Université Paris-Sud, 91405 Orsay, France*

(*Received* 4 *January* 1994; *accepted* 29 *March* 1995)

Abstract

Ab initio structure determination and refinement from electron diffraction data is not a widely used technique in structural science because of the inaccuracies inherent in the process of intensity measurement and because the relative sparseness of the data sets collected makes the structures hard to solve; there are also problems of verifying the correctness of the results. In this paper, the techniques of model building from electron diffraction data were employed to solve the structure. In addition, an *ab initio* solution of the structure of [9,9'-bianthryl]-10-carbonitrile is presented using a routine application of the maximum-entropy method combined with likelihood evaluation employing 150 unique diffraction intensities. The structure thus determined was obtained independently of the model-building studies. The agreement between the two methods is excellent and both agree with a single-crystal X-ray study on the same material. In addition, the high-resolution images agree with the images calculated from the model and with the potential maps after correction for the transfer function and dynamic scattering.

1. Introduction

A major problem for structure analysis of organic crystals, especially polymers, is their small dimensions, making X-ray methods inapplicable. On the other hand, some of the most interesting problems in materials development require detailed information about the direction of molecular dipoles or hyperpolarizabilities in thin films or small crystals. Therefore, knowledge of the molecular conformation and mutual orientation in the unit cell is essential, especially with a view to changing the molecular architecture in order to improve physical properties in a specific manner.

One solution to the problem lies in the improvement of the methods used in electron crystallography combined with high-resolution imaging. In this paper, we demonstrate a successful route to molecular modelling by simulating electron diffraction patterns from different projections. Most importantly, we show that the correct structure is obtained, although the *R* factor between simulated and experimental diffraction patterns is disappointingly bad by X-ray standards. This problem is well known and has been discussed repeatedly in the literature (Dorset, 1985*a,b*, 1991*a,b,c*, 1993; Dorset & McCourt, 1994). In addition, we adopt another approach to the problem of structure solution with the same experimental

data, using maximum-entropy phasing and likelihood evaluation (Bricogne, 1984, 1988*a,b*, 1991*a,b,c*, 1993; Bricogne & Gilmore, 1990). The potential maps obtained by this method are compared with theoretical and experimental high-resolution images after accounting for sample thickness and the contrast transfer function. Finally, the results are checked by X-ray single-crystal structure analysis and refinement. The excellent agreement between all four methods is a persuasive argument for the correctness of the structure determination and for the strength of the electron crystallography approach.

2. Material

The physico-chemical properties of the predecessor of the molecule investigated here, namely 9,9'-bianthryl (BA), have been investigated extensively in solution. For this molecule, it is well known that the two anthryl moieties are perpendicular to one another in the ground state and twisted by an angle of 70–78° in the first excited singlet state, caused by a double-minimum torsional potential (Yamasaki, Arita & Kajimoto, 1986). Cyanobianthryl was synthesized because a further improvement in the physico-optical properties was expected. A schematic drawing of 10-cyano-9,9'-bianthryl (CNBA) (IUPAC name: [9,9'-bianthryl]-10-carbonitrile) is shown in Fig. 1. As for BA, a perpendicular geometry was also found for CNBA in the S_0 state and a double-minimum potential in the S_1 state (Subaric Leihs, Monte, Roggam, Rettig, Zimermann & Heinze, 1990). However, this molecule is distinguished by its unusual photophysical properties, as was to be expected in view of its molecular architecture (Müller & Heinze, 1991; Elich, Lebius, Wortmann, Petzke, Detzer & Liptay, 1993; Wortmann, Elich, Lebius & Liptay, 1991). Of particular interest for the present investigations is the value of its dipole in solution and how this is related to its value in the crystalline phase. The final aim is to understand and optimize the properties of this class of molecule in the solid state with a view to second-harmonic generation.
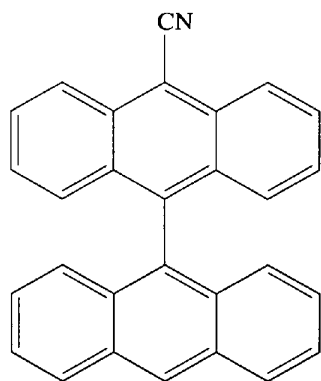

Fig. 1. Molecular geometry of 10-cyano-9,9'-bianthryl.

In solution, the dipole of CNBA has been determined experimentally to be 15.5×10^{-30} Cm (Wortmann, Elich, Lebius, Liptay, Borowicz & Grobowska, 1992), but its value in the solid state is expected to differ from this because it depends on the conformation of the molecule and the relative orientation of the molecules within the unit cell. In particular, its value with respect to macroscopic coordinates is required. This information can normally be obtained from X-ray structure analysis. However, it is important to develop electron crystallography and imaging of beam-sensitive organic materials for the following reasons:

(1) Organic and polymeric crystals are often too small for X-ray structure analysis. In some applications, thin films are required.

(2) The properties of many interesting organic materials are not well understood because there is insufficient information about typical defect structures.

Our efforts during the recent past have therefore been directed towards using and comparing several methods for *ab initio* structure analysis, using electron diffraction and high-resolution imaging (Voigt-Martin, Schumacher & Garbella, 1992, 1994; Voigt-Martin, Simon, Yan, Yakimansky, Baur & Ringsdorf, 1995; Voigt-Martin, Yan, Gilmore, Shankland & Bricogne, 1994; Voigt-Martin, Krug & Van Dyck, 1990).

3. Experimental methods

3.1. Electron diffraction

The samples were oriented by epitaxy on benzoic acid (Wittmann & Lotz, 1983). They formed small flat platelets with a thickness of 100–200 Å and were transferred to electron-microscope grids in the standard manner. They were investigated in the Philips EM420 STEM. The theoretical concepts related to electron diffraction are well known (Cowley, 1984, 1992). The main difficulties involved in practice are summarized below:

(1) The measured intensities are unreliable because inelastic and dynamic scattering affect the individual reflections independently and in a non-linear manner (*Pendellösung*) depending on sample thickness, which is usually unknown.

(2) Radiation damage may destroy or alter the crystal structure.

(3) In order to determine the space group and to obtain 3D data, a tilting series is essential but difficult to achieve before the sample is destroyed by the electron beam (Créwe, Isaacson & Zeitler, 1976; Henderson, & Glaser, 1985; Voigt-Martin, Schumacher & Garbella, 1992, 1994; Voigt-Martin, Simon, Yan, Yakimansky, Baur & Ringsdorf, 1995).

(4) Quantitative determination of the electron intensities from the photographic emulsion (Kodak SO 163) requires recording an exposure series in addition to

the tilt series because the linear region in photographic emulsions is limited. This is difficult to achieve with beam-sensitive samples.

(5) Many organic crystals and certainly most polymer crystals give rise to only a small number of reflections. This makes it very difficult to apply powerful direct phase methods, which normally require about five strong reflections per atom in the unit cell. However, encouraged by the recent successes in structure determination and refinement from electron diffraction data (Dorset, 1980, 1985a,b, 1990, 1991a,b,c, 1993; Dorset & McCourt, 1994; Voigt-Martin, Schumacher & Garbella, 1992, 1994; Voigt-Martin, Simon, Yan, Yakimansky, Baur & Ringsdorf, 1995; Voigt-Martin, Yan, Gilmore, Shankland & Bricogne, 1994; Voigt-Martin, Krug & Van Dyck, 1990), we have developed a new approach in which a number of techniques are combined, namely simulation of the electron diffraction patterns, *ab initio* structure determination by maximum-entropy and log-likelihood methods and high-resolution imaging. In the fortuitous situation to be described here, a complete X-ray structure analysis and refinement was also possible subsequently and confirmed the structure obtained by electron crystallography.

The crystals were transferred to electron-microscope grids in the usual manner and a suitable zone chosen for the tilting series. In order to obtain a good tilting series, relatively large but thin ($\sim$150 Å) defect-free regions of the sample were selected showing almost no bend contours. A rotation tilt holder is essential so that tilting about two suitable axes can be undertaken. For this sample, nine zonal projections were obtained.

Because the sample is extremely thin, the Fourier transform of the lattice function in the beam direction is not a δ function but has a Gaussian profile so that the precise tilt angle corresponding to a particular zonal projection is not well defined. However, a tilt series gives a better approximation for this angle. In addition, in the first step of analysis, the values of the cell constants obtained from the electron diffraction patterns is improved by comparison with an X-ray powder pattern (Voigt-Martin, Simon, Yan, Yakimansky, Baur & Ringsdorf, 1995; Cowley, 1988).

When the values of the cell constants have been optimized, the possible space groups are determined on the basis of systematic absences. In electron diffraction, these are often masked by the undesirable appearance of symmetry-forbidden reflections due to dynamical scattering or to structural effects in specific projections (Cowley, 1988; Gjonnes & Moodie, 1965). In addition, secondary scattering affects the intensities (Cowley, Rees & Spinks, 1951).

There is no general rule enabling easy detection and elimination of symmetry-forbidden reflections at the beginning of analysis. They can often be recognized in a tilting series and by their characteristic appearances as well as by comparison with the X-ray powder pattern.

Electron diffraction patterns are obtained in several zonal projections by successive tilting about appropriate crystallographic axes using the rotation/tilt holder in the goniometer stage of the electron microscope. When two prominent axes are found, then tilting both to the right and to the left about each axis gives the crucial information about the symmetry related to the zonal projections. From this series, a first approximation of the unit cell is possible and the observed extinctions and diffraction symmetry give the information about possible space groups. This information is used to index the powder X-ray pattern if this is available (Voigt-Martin, Simon, Yan, Yakimansky, Baur & Ringsdorf, 1995) and to improve the numerical values of the cell constants and angles as well as to recognize symmetry-forbidden reflections in the electron diffraction patterns.

3.2. Quantifying electron diffraction data

The electron diffraction intensities were quantified using the *ELD* system (Zou, Zukharev & Hovmöller, 1993). The electron diffraction pattern is transfered to an IBM 386 computer from a CCD camera *via* a frame grabber. The intensities were evaluated by the *ELD* software. The separate zones were merged into a single set by normalizing the common axis. These quantitative values are first compared with the kinematical values obtained from the model which is derived as described in §§ 4.6 and 4.7, to obtain the R_{kin} factor using the relationship $R = \sum_{hkl} ||F_o| - |F_c|| / \sum_{hkl} ||F_o||$ and *SHELX93* but incorporating electron scattering factors. If the sample is more than 50 Å thick, the dynamical scattering must be taken into account (Voigt-Martin, Krug & Van Dyck, 1990). The HRTEM module in *CERIUS* gives the *Pendellösung* plots for all reflections related to the model for different thicknesses and the appropriate intensities for different thicknesses can be extracted from them.

3.3. High-resolution imaging

High-resolution images were obtained from the same samples and investigated in a Philips 420 STEM in transmission mode. Organic samples have virtually no contrast and are beam sensitive. Low-dose imaging was therefore used to avoid beam damage. Contrast was obtained by using phase-contrast methods. The image is first viewed by using a CCD camera attached to the electron microscope and transferred to the *TIETZ VIPS* computer system. The Fourier transform of the image is calculated and the microscope parameters adjusted until the correct spatial frequencies are transferred into the electron microscope. The system is also used to optimize other microscope parameters such as astigmatism. Subsequently, an adjacent area that has not been exposed to the beam is photographed. In practice, another procedure is sometimes more convenient; the required contrast function to transfer the desired spatial

frequencies is calculated beforehand and adjusted, using carbon particles for focusing. Subsequently, an adjacent, previously unexposed, region is photographed.

Even organic samples, containing only light atoms, should have a thickness below 100 Å, otherwise dynamical scattering makes it difficult to interpret the image (Voigt-Martin, Krug & Van Dyck, 1990).

For these samples, it was found that good images could be obtained only in one specific projection, namely the one corresponding to the [010] zone diffraction pattern. The reason for this is clear when the results of simulation are considered (§ 3.8). These indicate that this is, in fact, a very favourable projection for imaging because one of the two anthracene moieties is perpendicular to the plane of the page (*i.e.* parallel to the electron beam).

3.4. *Improving the image*

The main problems arising in high-resolution electron microscopy of beam-sensitive organic samples are poor contrast and poor signal/noise ratio. The method selected to deal with this difficulty depends on the problem that has to be solved. In the case of a regularly repeated structure, averaging methods, both frequency filtering in reciprocal space (Predere, 1989; Voigt-Martin, Krug & Van Dyck, 1990) and image averaging in real space (Henderson, Baldwin, Ceska, Zemlin, Beckman & Downing, 1990), have been successfully used for many years. Appropriate software such as *MRC* was developed in Cambridge (Henderson & Unwin, 1975; Amos, Henderson & Unwin, 1982) and the *EMS* system in Martinsried (Hopper & Hegerl, 1980).

In this work, we used a more recent computer program *CRISP*, which is modelled on the *MRC* programs. The image was digitized by a standard CCD camera and transferred *via* a frame grabber to an IBM PC (Hovmöller, 1992). A fast-Fourier-transform routine calculates a 256 × 256 transform of the selected image area and the amplitude is displayed on the screen. Comparison of the diffractogram with the original electron diffraction patterns made it possible to determine the correct projection symmetry. The diffractogram exhibits, of course, a lower resolution than the electron diffraction pattern. Since the molecular modelling procedure (§§ 3.5, 3.6) indicates the conformation and orientation of the molecule in the unit cell for this projection, it is possible to decide which of the images had the most suitable projection for further processing and, indeed, which is most suitable for the subsequent maximum-entropy phasing procedure.

Finally, origin refinement based on the principles implemented in the *MRC* programs is performed (Amos, Henderson & Unwin, 1982; Hovmöller, 1992). First, a suitable symmetry centre is found and the phase residuals determined. Then *CRISP* automatically finds the position in the unit cell with the lowest phase residual. Subsequently, the constraints on amplitudes and phases corresponding to the determined symmetry are imposed.

Since all the necessary data are now available, the projected potential is calculated by an inverse Fourier transformation. This is compared with the projected potential calculated by molecular modelling and with the high-resolution images after taking account of the transfer function.

3.5. *Generation of a molecular model*

Conventional semi-empirical methods to calculate the conformation of molecules in the gas phase (CNDO, INDO, MNDO) have been used in quantum chemistry for many years (Pople, Beveridge & Dabosh, 1967; Dewar & Yamaguchi, 1978; Bingham, Dewar & Lo, 1975; Thiel & Dewar, 1977; Dewar, Zoebisch, Healy & Stewart, 1985; Stewart, 1989). The most advanced of them, MNDO (Dewar & Yamaguchi, 1978), is known to suffer from an overestimation of the repulsion between atoms when they are about a van der Waals distance apart.

Good results were initially produced with *AM*1, in which the core repulsion function (CRF) was modified by additional Gaussian terms (Dewar, Zoebisch, Healy & Stewart, 1985). In a further optimization of parameters (such as heat of formation, dipole moments, ionization potentials), the program *MNDO-PM*3 was used, which is incorporated in the program package *MOPAC*6.0 (Stewart, 1989). There are always several minimum-energy conformations. As a first approximation, the conformation that can be fitted into the experimentally determined unit cell is chosen.

3.6. *Simulation of the electron diffraction patterns*

In order to proceed with simulations, the crystal unit cell and space group are required. The information was obtained from the electron diffraction data. Generally, several space groups can be postulated on the basis of the observed extinctions. The number can be reduced when the symmetry requirements of the molecule are taken into account. For simulation, the *MOPAC*-calculated molecule is placed into the unit cell using *CERIUS* so that the required symmetry of both molecule and space group are satisfied and agree with the observed extinctions and symmetry. Because the changing diffraction pattern as the molecule is adjusted is immediately displayed in *CERIUS*, a first qualitative agreement and a good value for the density can be achieved within a reasonable time. At this stage, the packing energy is usually positive and a number of non-allowed close contacts are observed. These can be eliminated by suitably adjusting the geometrical parameters in the *Z* matrix. Subsequently, the *CRYSTAL PACKER* in *CERIUS* is used to ensure that the packing energy of the

crystal is negative and non-allowed contacts eliminated while retaining the correct symmetry. At this stage, adjustments to the molecular conformation arising from the crystal field are undertaken and the energy again minimized, still retaining the correct symmetry.

3.7. *The crystal packer*

In order to ensure that the crystal packing energy is negative, the *CERIUS CRYSTAL PACKER* module was used. The potential energy of the crystal is written as the superposition of various two-body, three-body and four-body interactions:

$$E = E_{vdw} + E_{coul} + E_{hb} + E_{torsion}.$$

(I) The van der Waals term is treated using the Lennard-Jones functional form; (II) the Ewald summation technique is used to calculate the Coulomb energy (Karasawa & Goddard, 1989); (III) the energy of the hydrogen bonds is calculated using the CHARM-like potential; (IV) a Dreiding force field is used for the calculation of subrotation interactions (Mayo, Olafson & Goddard, 1990).

Negative packing energies can always be found for several structures but comparison with the experimental diffraction patterns, especially if several zones are available, generally reduces them to a unique solution.

3.8. *Simulation of the image*

The image is calculated in the HRTEM mode of *CERIUS* using the atomic coordinates determined as described in §§ 3.6 and 3.7. The images calculated by *CERIUS* are obtained in several steps using the multislice method (Cowley, 1984). The programs were developed by Saxton (1983).

3.9. *Ab initio structure determination using the ME method*

Traditional direct methods of structure solution have been used for some years in electron crystallography. They can be successful but, in general, they need tighter control than needed for data sets derived from single-crystal X-ray diffraction (Dorset, 1991*a,b,c*, 1993; Dorset & McCourt, 1994; Fan, Zhong, Zheng & Li, 1985; Han, Fan & Li, 1986; Liu, Fan & Zheng, 1988). The reason for the problem is that traditional direct methods require:

(1) a data resolution of 1.1–1.2 Å;

(2) a nearly complete sampling of reciprocal space to this resolution;

(3) reasonably accurate intensity measurements devoid of large systematic errors.

These criteria cannot be met with most electron diffraction data sets: in general, the data are obtained from a tilting series with a maximum tilt angle of 60° and thus incompletely span reciprocal space; often a

resolution of 1.1–1.2 Å is difficult to achieve, and large systematic errors exist in the intensity measurements as a consequence of dynamical and incoherent scattering.

The maximum-entropy (ME) phasing method is, however, not so constrained in terms of data quality and can, therefore, have a valuable role to play in electron crystallography. The underlying theory, on which this work is based, has been described in detail elsewhere (Bricogne, 1984, 1988*a,b*, 1991*a,b,c*). As in standard direct methods (Hauptman & Karle, 1953), it starts with an unknown crystal structure made up of atoms of known chemical type, but unknown position, which are considered random with an initially uniform distribution in the asymmetric unit of the crystal. Structure determination consists, of course, in the removal of that randomness. Just as in traditional direct methods, probability limit theorems are used to estimate the joint probability distribution of suitably chosen structure factors; the substitution of the observed structure factor into these distributions yields conditional joint distributions for the phases, indicating that certain combinations of phase values are more probable than others once the amplitudes are known.

However, the traditional ways of doing this involving the Gram–Charlier or Edgeworth series (Cramer, 1946; Klug, 1958) or related expressions (Hauptman & Karle, 1953) are not used. Instead, the saddle-point method (Daniels, 1954) is invoked. This is equivalent to requiring the distribution of random atomic positions to be updated whenever phase assumptions are made so as to retain maximum entropy under the constraints embodied in these assumptions. This approach to the phase problem leads naturally to a general multisolution strategy of structure determination (Bricogne, 1984, 1988*b*; Bricogne & Gilmore, 1990) in which the space of hypothetical phase sets is explored in a hierarchical fashion by building a phasing tree. Each trial phase set is represented as a node on the tree and is ranked according to the log-likelihood gain (LLG) or the Bayesian score associated with it, which, in turn, measures how well a trial phase choice predicts the pattern of observed unphased intensities *via* the process of maximum-entropy extrapolation. The growth of the phasing tree is guided and controlled throughout by this heuristic function.

For the purposes of *ab initio* phasing from electron diffraction, the method is implemented as follows (Bricogne & Gilmore, 1990; Gilmore, Bricogne & Bannister, 1990; Gilmore & Bricogne, 1992):

(1) The diffraction intensities are normalized using electron scattering factors to give unitary structure factors, $|U_h|^{obs}$. For sparse data sets, such as one has for electron diffraction, this can be a problematic procedure and often one has to impose a positive overall temperature factor: there is a tendency for sparse data sets to produce negative values of this parameter.

(2) An origin (and enantiomorph, if relevant) is defined by fixing the phases of suitable reflections. This is
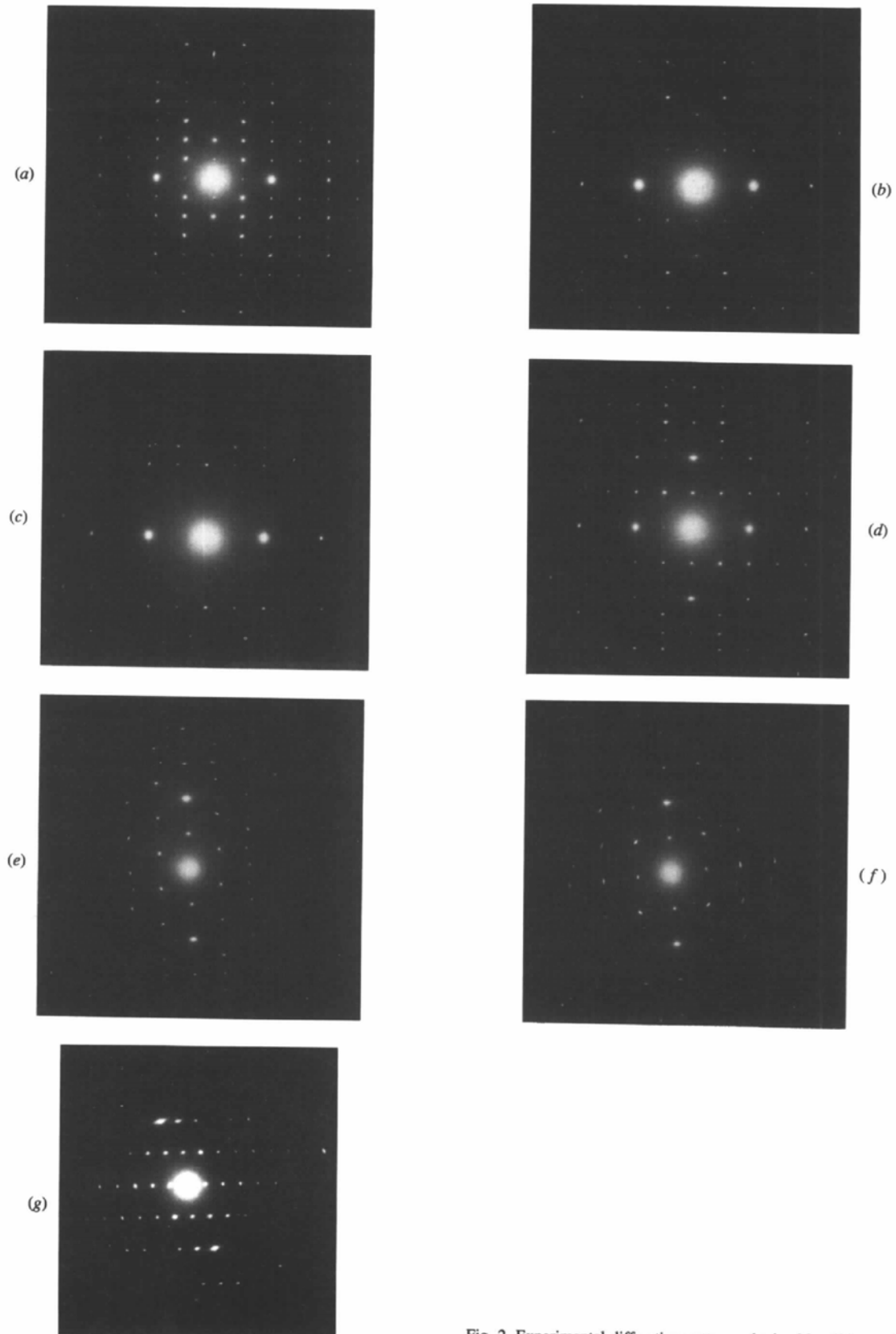
Fig. 2. Experimental diffraction patterns obtained by tilting series.

carried out automatically by the *MICE* program using a second-neighbourhood search procedure (Bricogne, 1993). These phased reflections form a basis set {H} and are used as constraints in an entropy-maximization procedure employing a highly modified exponential modelling scheme (Bricogne, 1984; Bricogne & Gilmore, 1990). This generates the root node of a phasing tree. The properties of the maximum-entropy map, $q^{ME}(x)$, thus produced are such that it is capable of extrapolating new phase and intensity information, *i.e.* it is capable of phase determination.

(3) At this point, however, the extrapolation usually is too weak to be of any value and new phase information needs to be incorporated into the basis set. This is carried out by adding new strong reflections, which are hitherto inconclusively extrapolated, by permuting their phases. This gives rise to a series of phase choices and each choice is represented as a node on the second level of the phasing tree. The reflections that are chosen are those that optimally enlarge the second neighbourhood of the basis set (Bricogne, 1993). The latter consists of those reflections $h_1 \pm 'R_g \cdot h_2$ for $h_1, h_2 \in H$, where $'R_g$ is the transpose of a rotation matrix of the space group.

(4) Each node is subjected to constrained entropy maximization to produce a revised non-uniform distribution for the random atomic positions. To rank the nodes, a Rice-type likelihood function is used (Bricogne, 1984, 1988*b*; Bricogne & Gilmore, 1990), which evaluates the agreement between the extrapolated structure-factor magnitudes from the relevant maximum-entropy distribution and the experimentally measured values. This criterion measures the extent to which the observed pattern of the unphased intensities has been rendered more likely by the phase choices made for the reflections in the basis set (with a hypothesis H_1 specified) than they were under the null hypothesis H_0 of uniform distribution of these random positions. The log-likelihood gain (LLG) is defined as a sum of logarithms of probability ratios calculated under the two hypotheses for a sample of observed values of structure-factor amplitudes in the second neighbourhood of the basis set, as defined in (4) above.

(5) The LLG's are analysed for phase indications using the Student t test (Bricogne, 1993; Shankland, Gilmore, Bricogne & Hashizume, 1993). The simplest test involves the detection of the main effect associated with the sign of a single phase. The LLG average, μ^+, and its associated variance V^+ is computed for those nodes in which the sign of the phase under test is +. The calculation is then repeated for those nodes in which the same sign is − to give the corresponding μ^-, and variance V^-. These parameters are used in a Student t test, which defines the significance level of the contrast in the two means as the probability that it could arise solely from the fluctuations measured by V^+ and V^- (even if the two distributions of LLG had the same theoretical mean). This enables sign choices to be made

with an associated significance level. This calculation is repeated for all the single-phase indications and is then extended to combinations of two and three phases. An extension to acentric phases is straightforward by employing two signs to define the phase quadrant both in permutation and in the subsequent analysis. In general, significance levels of 2% are used, but this is sometimes relaxed with sparse data sets.

(6) Only those nodes that are consistent with the t-test results are kept, further pruned if necessary to 8–16 in a given level. Further reflections are then permuted and a new level of nodes generated. This procedure is continued until most large unitary structure factors have significant phase indications.

(7) The ME distributions associated with the various nodes are not electron potential maps in the traditional sense. The latter are generated as centroid maps (Bricogne & Gilmore, 1990) by means of a Sim-type filter (Sim, 1959).

The method has been very successful with electron diffraction data sets from perchlorocoronene (Dong, Baird, Fryer, Gilmore, MacNicol, Bricogne, Smith, O'Keefe & Hovmöller, 1992), a variety of organic and inorganic molecules (Gilmore, Shankland & Bricogne, 1993), and phase extension from Purple Membrane (Gilmore, Shankland & Fryer, 1992).

3.10. *X-ray structural analysis*

The cyanobianthryl was dissolved in Me_2SO solution and allowed to crystallize for several months. The structure was solved by direct methods using *SHELXS*86 (Sheldrick, 1986) and refined by full-matrix least-squares analysis using *SHELX*76 (Sheldrick, 1976). Lorentz and polarization corrections were applied using a local data-reduction program. Non-H atoms were refined anisotropically. H atoms were located from difference Fourier maps and refined isotropically.

4. Results

4.1. *Electron diffraction and simulation*

A series of selected-area diffraction patterns from CNBA are shown in Fig. 2 using an area of about $3 \times 3 \, \mu m$. The diffraction pattern of Fig. 2(*d*) contains two strong perpendicular axes. Initially, we refer to this as the basic zone. Tilting about the horizontal axis until the next zone appears produces the diffraction patterns in Figs. 2(*a*)–(*c*). Tilting about the vertical axis produces the diffraction patterns in Figs. 2(*e*)–(*f*). The diffraction pattern in Fig. 2(*g*) was obtained fortuitously when a crystal was found in this orientation. From this series of diffraction patterns and the experimental tilt angles, a unit cell was defined as follows: For tilt axis b^*, the crystallographic (101)* zone appeared at 27°, (201)* at 0°, (301)* at −10°, (401)* at −16, (501)* at −19° and

$(100)^*$ at $31°$. When tilted about the other axis, which emerged as being [102], two further zones appeared, namely $(211)^*$ at $20°$ and $(221)^*$ at $33°$. From the analysis, it emerges that Fig. 2(g) shows the [010] zone; $\mathbf{a}^*$ and $\mathbf{c}^*$ are clearly not perpendicular but are inclined at an angle of $68°$. An initial unit cell can be postulated from these experiments: $a = 14.70$, $b = 9.47$, $c = 15.42$ Å, $\beta = 112°$ and all the diffraction spots indexed. A simple powder X-ray diffraction pattern was then used to check the d values and indices as described previously (Voigt-Martin, Yan, Wortmann & Elich, 1995). In order to obtain a density of about $1 \, \mathrm{g \, cm^{-3}}$, there had to be 4 molecules in the unit cell.

The systematic absences were consistent with space group $P2_1/c$.

4.2. High-resolution images and data processing

Good high-resolution images were obtained only in the ac projection (Fig. 3). A series of elliptical objects arranged in lines with an included angle of $81°$ are observed.
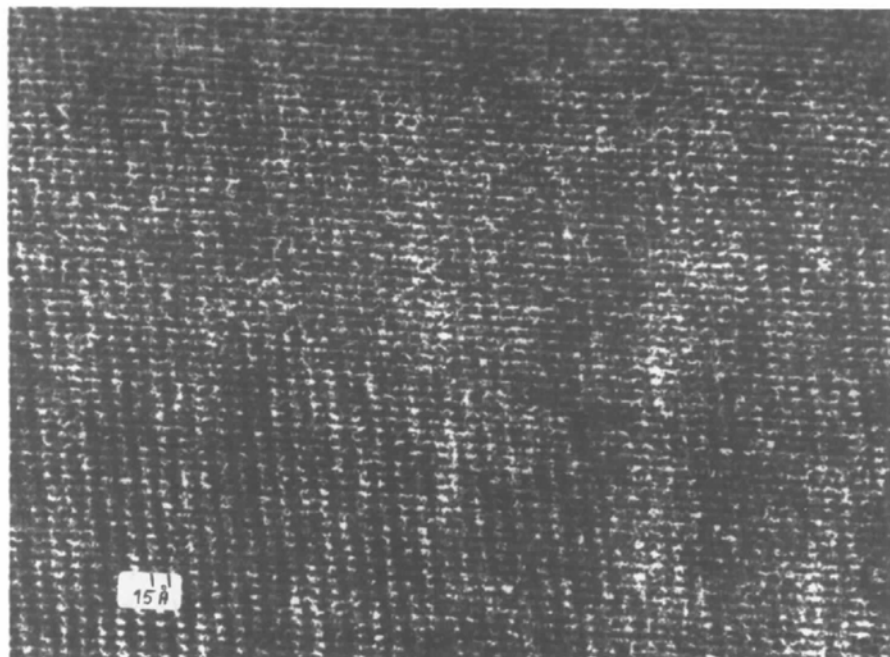

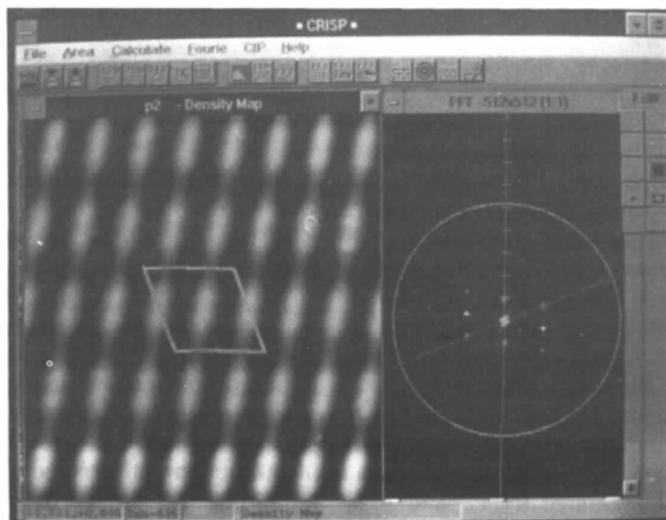Fig. 3. High-resolution image of 10-cyano-9,9'-bianthryl in ac projection.

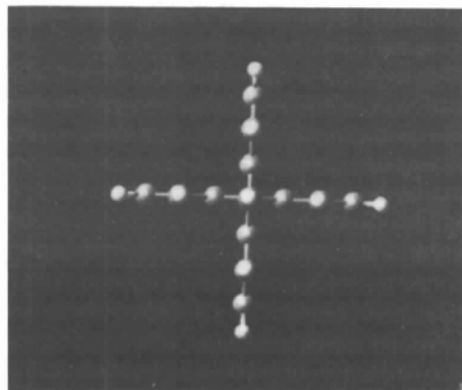Fig. 4. Image-processing procedure by *CRISP*.

A Fourier transform of the image reveals a low-resolution diffractogram of the [010] zone, which was then used in the *CRISP* procedure to improve the image as indicated in Fig. 4.
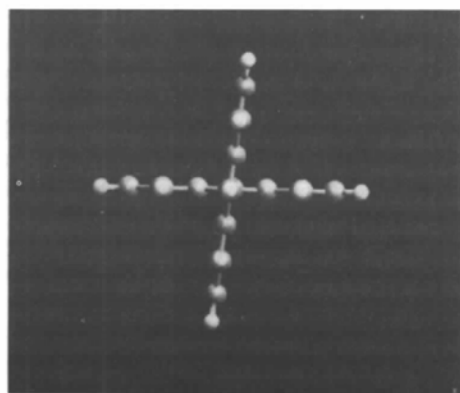
4.3. *Generation of molecular model*

Semi-empirical calculations of the torsional potential energy as well as the dipole moment and hyperpola-
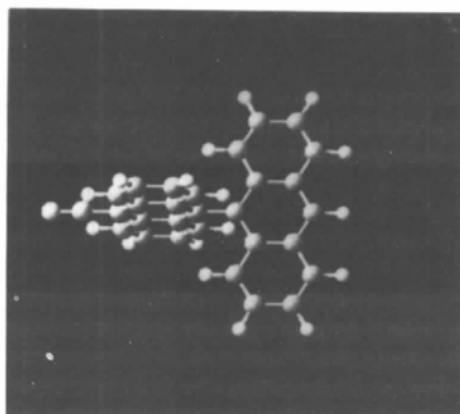
(*a*)

(*b*)

(*c*)

Fig. 5. (*a*) Conformation of CNBA molecule. Projection showing angle between anthracene moieties (*b*) in gas phase, (*c*) in crystalline phase.

Table 1. *Bond lengths* (Å)

	X-ray	MOPAC		X-ray	MOPAC
C1—C2	1.408	1.424	C15—C16	1.364	1.364
C1—C14	1.354	1.365	C15—C28	1.412	1.425
C2—C3	1.347	1.365	C16—C17	1.409	1.433
C3—C4	1.439	1.433	C17—C18	1.398	1.398
C4—C5	1.395	1.408	C17—C26	1.437	1.428
C4—C13	1.430	1.428	C18—C19	1.377	1.398
C5—C6	1.412	1.408	C19—C20	1.441	1.433
C5—C29	1.462	1.423	C19—C24	1.441	1.429
C6—C7	1.423	1.433	C20—C21	1.336	1.364
C6—C11	1.434	1.428	C21—C22	1.413	1.425
C7—C8	1.356	1.365	C22—C23	1.372	1.365
C8—C9	1.416	1.424	C23—C24	1.419	1.434
C9—C10	1.344	1.365	C24—C25	1.418	1.409
C10—C11	1.443	1.434	C25—C26	1.397	1.408
C11—C12	1.397	1.408	C26—C27	1.432	1.434
C12—C13	1.413	1.409	C27—C28	1.346	1.365
C12—C25	1.503	1.473	C29—N1	1.123	1.164
C13—C14	1.431	1.434			

rizability as a function of torsional angle were carried out using both *AM*1 (Bingham, Dewar & Lo, 1975) and *MNDO-PM*3 calculations (Stewart, 1989). The calculated parameters were compared with the results of density, refractometry and permittivity measurements and free-jet experiments. The geometry of the molecule was fully optimized at a fixed value of the torsional angle. Good correspondence was found between the potential calculated by the *AM*1 method and those obtained from the evaluation of the torsional level spacings in the free-jet experiments (Müller & Heinze, 1991). The results of these experiments and calculations indicated that the minimum-energy torsional angle φ_{min} between the anthracene moieties in the gas phase and in solution in the S_0 state is 90°. While the *AM*1 calculations indicate a very flat energy minimum around 90°, the *PM*3 method predicted a steeper rise. The calculated values of the dipole for this conformation was 13.1×10^{-30} Cm, only slightly lower than the experimental value of 15.5×10^{-30} Cm. A model of the molecule in the minimum-energy conformation is shown in Fig. 5. Some *MOPAC*-calculated values of bond lengths are given in Table 1.

4.4. *Simulation of electron diffraction pattern and packing considerations*

The *MOPAC*-calculated molecule was placed in the $P2_1/c$ unit cell that had been determined experimentally as described in § 5.1 using *CERIUS*. At this stage, the criteria that must be satisfied are:

(1) the calculated and experimental diffraction patterns must be qualitatively equal in all zones;

(2) the density should be about 1 g cm^{-3};

(3) the symmetry of both molecule and unit cell must satisfy the requirements dictated by the observed extinctions.

Subsequently, the packing energy was minimized with *CRYSTAL PACKER* and non-allowed close contacts eliminated. The density of this unit cell was 1.3 g cm^{-3}.

Initially, the equilibrium torsional angle between the anthracene moieties was kept at 90° because this value agrees with those obtained by laser-induced fluorescent spectroscopy. However, from the *AM*1 data, the torsional potential in the vicinity of 90° is rather flat. Therefore, one can expect the crystal field to affect this value. Indeed, the results indicate that, with this molecular geometry, under optimal packing conditions, there are unsuitably close contacts of 3.32 Å between C atoms, and that a better result can be obtained with a torsional angle of about 83°. In the subsequent analysis of crystal structures and crystal energies, both angles were considered in detail. The charge distribution within the CNBA
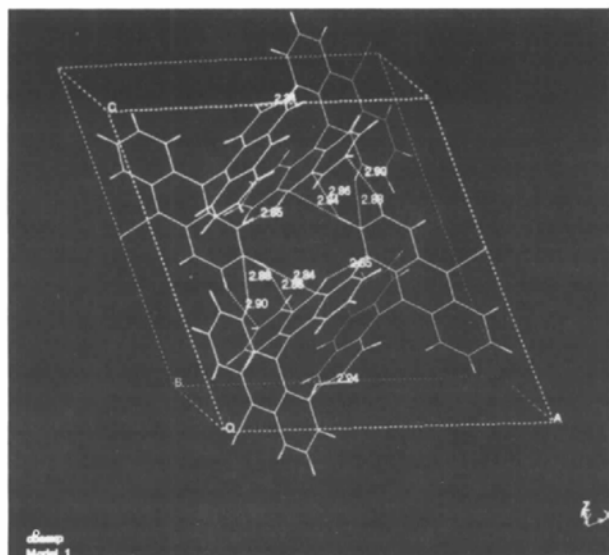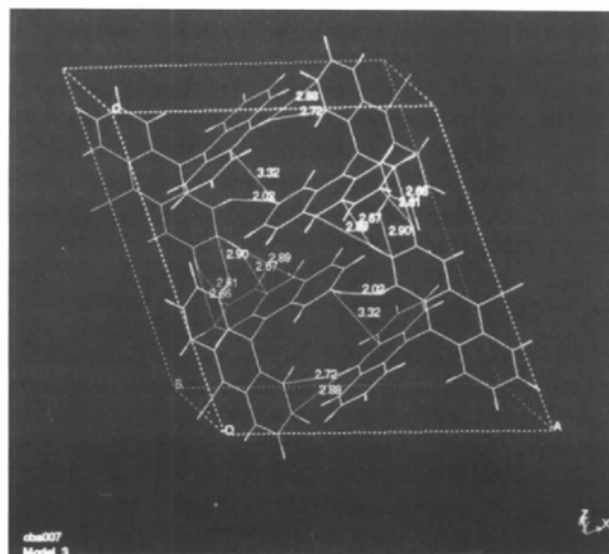
Table 2. *Van der Waals and Coulomb contributions to total energy* (kJ mol^{-1}) *per cell*

Structure	wdW	Coulomb	Total
I	−624.7	−40.2	−664.9
II	−455.1	−46.9	−502.0

I: Experimental crystal structure with torsion angle 83–85°. Charge distribution is calculated for the isolated CBA molecule 'extracted' from the experimental crystal lattice.

II: Hypothetical crystal structure with torsion angle 90°. Crystal energy was optimized at the same crystal cell parameters as for the experimental crystal structure. Charge distribution is calculated for the isolated CBA molecule with equilibrium torsion angle 90°.

molecules in the crystal cell was initially taken from the *MOPAC* data for the isolated molecule at 90° because one does not expect a remarkable change in charge distribution when the torsional angle is decreased from 90 to 83°. Furthermore, as will be shown below, the total crystal energy is dominated by the van der Waals, rather than by the electrostatic, contribution.

The model structure for torsional angles of 83 and 90° are shown in Figs. 6(*a*) and (*b*), respectively, using the same crystal cell parameters. The figure shows the close contacts between the atoms of different molecules in the cell. It is immediately clear that the number of unfavourable close contacts is much lower at 83 than at 90°. Moreover, at 83°, there are no undesirable contacts between the heavier atoms (C–C and C–N). For this reason, the value of the van der Waals contribution to the total crystal energy for a torsional angle of 83° is much lower than that at 90° (Table 2), while the Coulomb contribution is hardly affected.
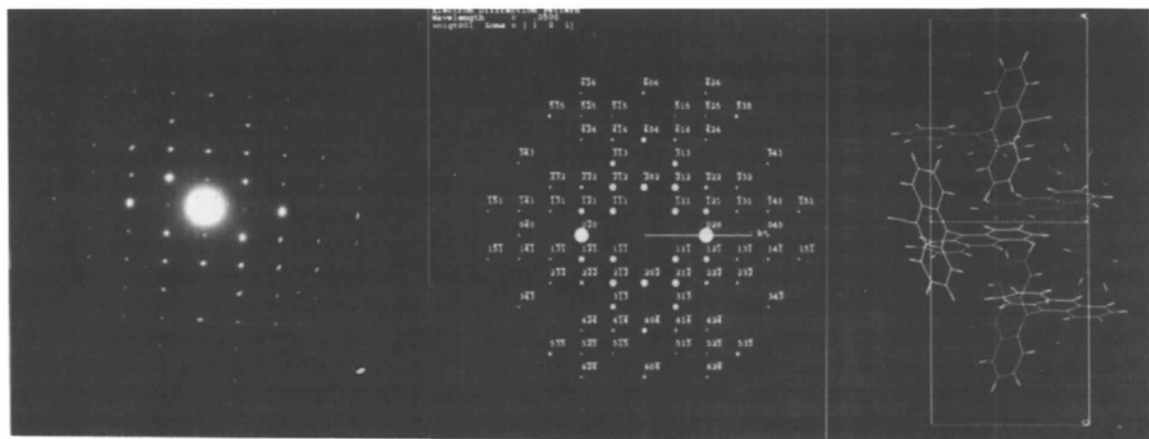
4.5. *Comparison between calculated and experimental diffraction patterns*

In Fig. 7(*a*)(i), the calculated kinematical diffraction patterns based on the molecular model with a torsional angle of 83° are compared with the experimental diffraction patterns in nine different zones. It is clear that qualitatively the agreement is excellent in all cases.

Quantitatively, the agreement is less satisfactory (see Table 3). From these values, an *R* factor of 0.35 between experimental and calculated intensities was obtained. Although this value would be completely unsatisfactory in X-ray diffraction, it is within the range that has been achieved in recent years by direct phase methods in electron crystallography (Dorset, 1980, 1985*a,b*, 1990, 1991*a,b,c*). These poor *R* factors are caused by dynamical and incoherent scattering. For dynamical scattering, the intensity of each maximum is described by a *Pendellösung Ansatz* and its value depends on thickness (Fig. 8). As we have derived previously on a theoretical basis (Voigt-Martin, Krug & Van Dyck, 1990), the non-linearity is considerable at thicknesses above 50 Å, even for organic samples. Ideally, it should therefore be possible to derive dynamical *R* factors and to monitor

(*a*)

(*b*)

Fig. 6. Molecular packing in unit cell with (*a*) torsional angle $\varphi = 90°$, (*b*) $\varphi = 83°$.
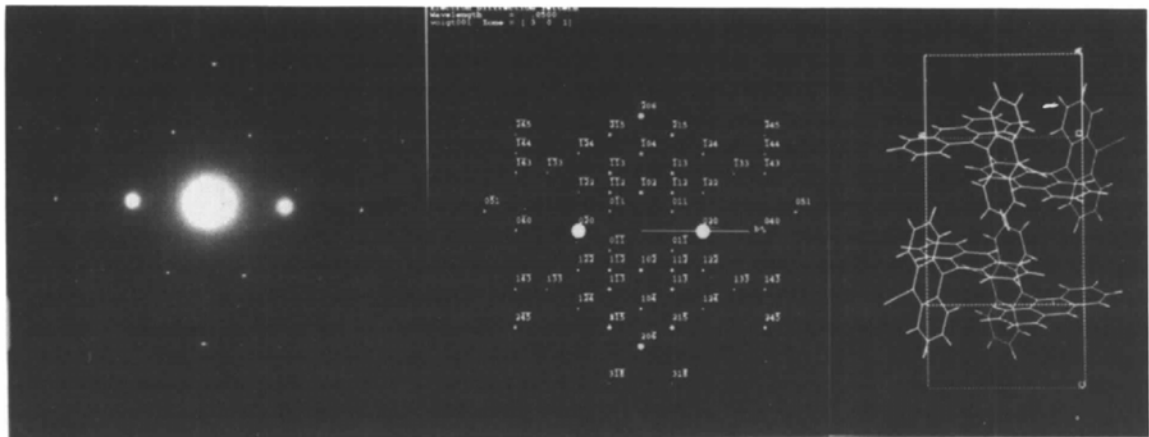
(a)

(b)

(c)

(i)   (ii)   (iii)

Fig. 7. (*a*)–(*c*) Tilting series showing agreement between experimental and simulated electron diffraction patterns of CNBA in (301)*, (201)* and (010)* zones with corresponding projections in simulated models (*CERIUS*3.0). (*d*)–(*f*) Tilting series showing agreement between experimental and simulated electron diffraction patterns of CNBA in (201)*, (211)* and (020)* zones with corresponding projections in simulated models (*CERIUS*3.0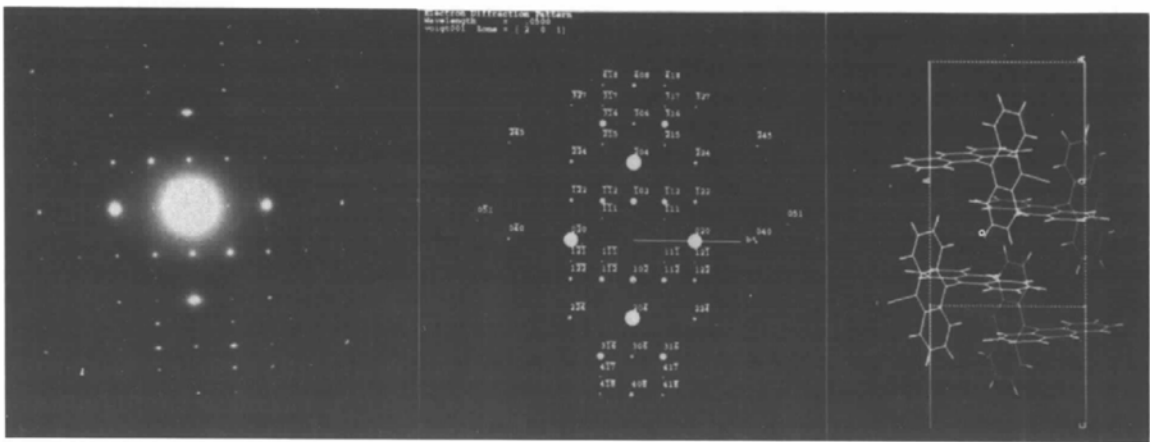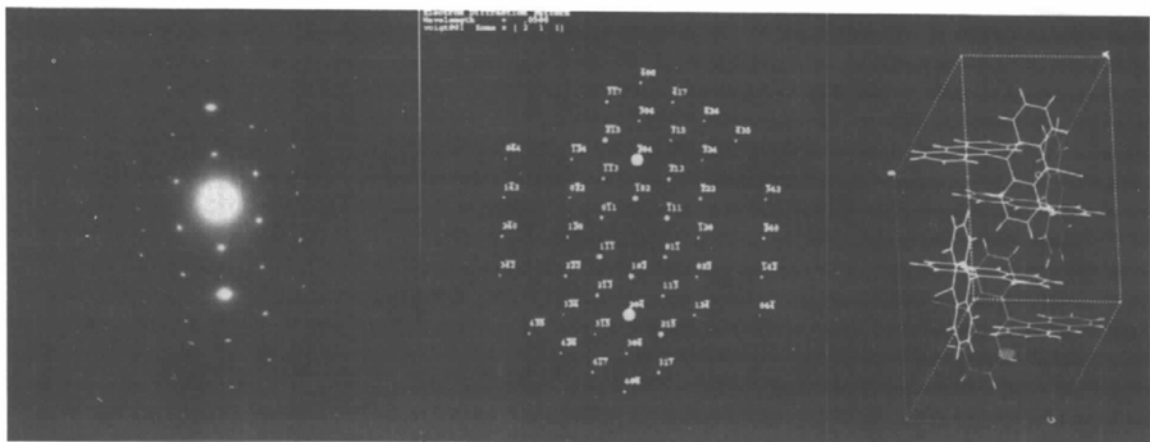). (*g*)–(*i*) Tilting series showing agreement between experimental and simulatd electron diffraction patterns of CNBA in (100)*, (401)* and (501)* zones with corresponding projections in simulated models (*CERIUS*3.0).

(d)

(e)

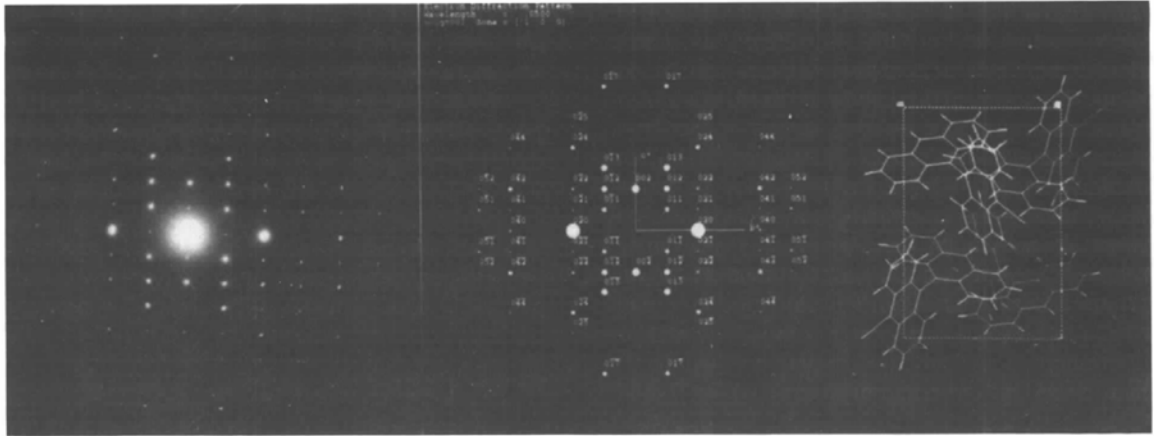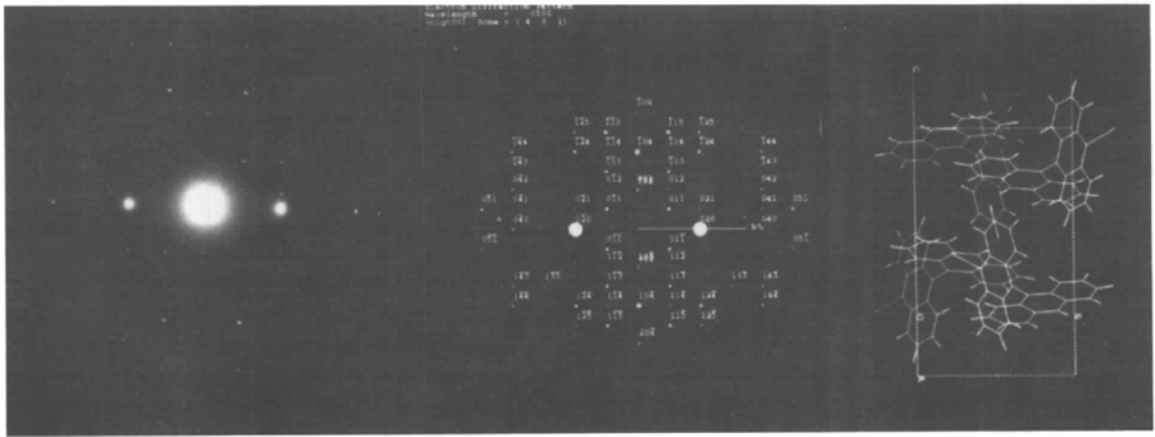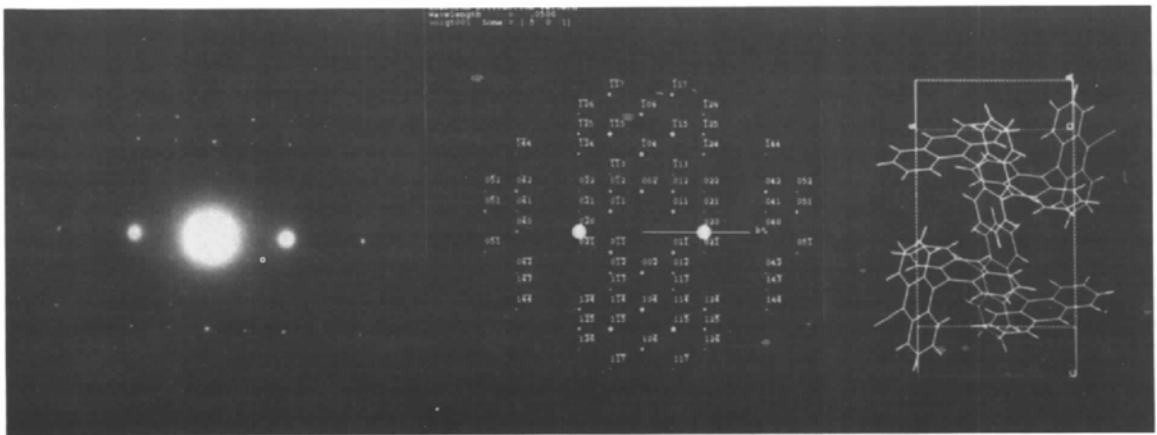(f)

(i)   (ii)   (iii)

Fig. 7. (cont.)

(g)

(h)

(i)

(i)   (ii)   (iii)

Fig. 7. (*cont.*)

Table 3. *Intensities at* 100 Å *thickness*

h	k	l	$I_{kin}^{1/2}$	$I_{exp}^{1/2}$	$I_{dyn}^{1/2}$	h	k	l	$I_{kin}^{1/2}$	$I_{exp}^{1/2}$	$I_{dyn}^{1/2}$
0	2	0	491.93	397.82	629.77	−1	5	2	44.72	47.63	15.74
0	4	0	86.60	114.90	87.46	−2	0	4	525.26	400.10	577.29
0	6	0	128.06	68.84	34.98	−2	1	4	26.45	57.45	69.97
0	1	1	148.66	156.66	146.95	−2	2	4	117.47	73.23	122.45
0	2	1	60.00	71.25	69.97	−2	3	4	17.32	45.41	27.99
0	3	1	24.49	82.28	244.91	−2	4	4	22.36	57.45	5.94
0	4	1	58.31	75.86	62.97	−2	5	4	36.05	49.75	6.99
0	5	1	102.47	82.28	52.48	−3	0	6	104.40	76.00	164.44
0	0	2	536.66	169.63	314.88	−3	1	6	242.49	114.90	237.91
0	1	2	186.82	128.79	244.91	−3	2	6	37.41	53.74	90.96
0	2	2	93.27	81.24	69.97	−3	4	6	194.68	86.17	87.46
0	3	2	10.00	78.06	59.47	−3	5	6	10.00	53.74	3.49
0	4	2	170.59	98.22	146.95	−4	0	8	143.53	62.60	34.98
0	5	2	72.11	55.19	34.98	−4	1	8	70.71	60.93	45.48
0	1	3	231.95	115.64	276.40	−4	3	8	34.64	32.11	3.49
0	2	3	10.00	65.05	31.48	−4	4	8	80.62	38.00	11.89
0	3	3	26.45	72.43	41.98	−5	0	10	74.83	40.62	10.49
0	4	3	28.28	58.18	45.48	−5	1	10	41.23	40.62	17.49
0	0	4	37.41	67.60	69.97	−1	1	3	126.10	100.17	160.94
0	1	4	10.00	63.73	45.48	−1	2	3	24.49	51.38	24.49
0	2	4	154.92	92.91	139.95	−1	3	3	56.56	68.94	62.97
0	3	4	20.00	52.04	41.98	−1	4	3	76.81	72.67	55.97
0	4	4	72.11	74.73	55.97	−1	5	3	125.70	79.60	4.54
0	1	5	22.36	68.84	17.49	−2	0	6	213.31	130.00	122.45
0	2	5	51.96	73.59	66.47	−2	1	6	36.05	60.80	69.97
0	3	5	37.41	66.33	41.98	−2	2	6	22.36	68.94	55.97
0	0	6	10.00	52.04	34.98	−2	4	6	77.46	72.67	31.48
0	1	6	46.90	26.02	34.98	−2	5	6	84.85	64.99	2.79
0	2	6	36.05	55.19	17.49	−1	0	4	177.20	91.84	111.96
0	3	6	17.32	31.86	24.49	−1	1	4	50.99	42.82	94.46
0	1	7	182.21	97.36	136.45	−1	2	4	112.25	54.16	111.96
0	3	7	90.55	63.73	31.48	−1	3	4	17.32	46.90	27.99
0	0	8	114.46	68.84	38.48	−1	4	4	73.48	50.66	59.47
0	1	8	59.16	34.42	31.48	−2	0	8	10.00	93.81	10.49
−1	1	1	220.00	182.10	297.39	−2	1	8	10.00	19.15	6.99
−1	2	1	197.23	74.90	178.43	−2	2	8	51.96	19.15	15.74
−1	3	1	81.85	51.38	75.22	−2	3	8	20.00	27.08	13.99
−1	4	1	85.44	57.45	66.47	−1	1	5	163.71	132.01	143.45
−1	5	1	87.75	48.06	55.97	−1	2	5	92.19	45.96	97.96
−1	6	1	74.83	33.98	34.98	−1	3	5	20.00	51.38	17.49
−2	0	2	234.73	152.54	227.42	−1	4	5	26.45	72.67	27.99
−2	1	2	241.04	137.76	293.89	−1	5	5	43.58	45.96	4.89
−2	2	2	130.77	77.07	153.94	−5	1	9	156.52	38.73	48.98
−2	3	2	84.85	67.97	125.95	−5	2	8	75.49	32.40	20.99
−2	4	2	31.62	49.75	34.98	−5	4	6	186.28	17.32	59.47
−2	6	2	31.62	18.16	6.99	−4	1	7	121.24	48.99	69.97
−3	1	3	190.53	101.15	174.93	−4	2	6	95.39	32.40	24.49
−3	2	3	24.49	49.75	31.48	−4	3	5	123.29	21.21	87.46
−3	4	3	77.46	54.50	73.47	−3	1	5	91.65	80.32	150.44
−3	5	3	14.14	36.33	6.29	−3	2	4	62.45	40.62	108.46
−3	6	3	24.49	18.16	6.99	−3	4	2	106.30	36.74	80.47
−4	0	4	172.34	96.99	262.40	−3	5	1	14.14	34.64	17.49
−4	1	4	101.98	57.45	139.95	−2	1	3	157.16	73.49	192.43
−4	2	4	77.46	60.25	87.46	−2	3	1	28.28	32.40	55.97
−4	3	4	36.05	48.06	55.97	−2	4	0	115.76	50.50	115.46
−4	4	4	30.00	46.31	27.99	−2	5	−1	125.70	44.16	34.98
−5	1	5	59.16	55.99	94.46	−1	2	0	98.99	50.50	115.46
−5	2	5	67.08	48.06	94.46	−1	3	−1	20.00	34.64	41.98
−5	3	5	142.83	60.25	94.46	−1	4	−2	117.90	36.74	69.97
−5	4	5	17.32	31.46	13.99	−1	5	−3	10.00	12.24	10.49
−5	5	5	107.24	46.31	15.74	0	5	−5	10.00	17.32	3.49
−6	0	6	116.62	61.60	150.44	1	4	−6	43.58	42.43	27.99
−6	2	6	84.85	46.31	34.98	2	1	−5	229.13	48.99	244.91
−6	3	6	43.58	31.46	13.99	2	3	−7	45.82	38.73	22.74
−6	4	6	10.00	49.75	3.49	4	0	4	14.14	49.66	6.99
−6	5	6	79.37	12.84	6.99	5	0	4	62.45	64.12	13.99
−7	1	7	107.24	42.60	41.98	6	0	4	56.56	49.66	6.64
−1	0	2	224.72	172.35	279.90	−5	0	6	303.64	288.19	157.44
−1	1	2	186.82	166.26	209.92	−4	0	6	80.62	271.03	76.97
−1	2	2	125.30	101.56	139.95	−1	0	6	142.83	68.26	87.46
−1	3	2	40.00	57.45	69.97	2	0	6	17.32	52.35	24.49
−1	4	2	30.00	60.93	59.47	3	0	6	30.00	111.06	3.49

Table 4. *Atomic coordinates obtained by simulation*

C1	0.28699	0.57964	−0.02141
C2	0.21161	0.48306	−0.07156
C3	0.15061	0.42888	−0.03137
C4	0.16089	0.46765	0.06163
C5	0.09867	0.41286	0.10421
C6	0.10997	0.45228	0.19568
C7	0.04744	0.39772	0.24027
C8	0.05947	0.43714	0.32901
C9	0.13484	0.53373	0.37914
C10	0.19578	0.58778	0.33888
C11	0.18563	0.54917	0.24581
C12	0.24811	0.60435	0.20360
C13	0.23643	0.56448	0.11206
C14	0.29891	0.61892	0.06730
C15	0.28184	1.14520	0.21548
C16	0.36905	1.09559	0.27691
C17	0.38607	0.94700	0.29184
C18	0.47528	0.89543	0.35466
C19	0.49151	0.75038	0.36897
C20	0.58278	0.69694	0.43329
C21	0.59815	0.55526	0.44694
C22	0.52312	0.45784	0.39705
C23	0.43529	0.50496	0.33526
C24	0.41614	0.65300	0.31889
C25	0.32611	0.70429	0.25547
C26	0.31021	0.85055	0.24137
C27	0.21965	0.90710	0.17748
C28	0.20597	1.04927	0.16503
C29	0.02335	0.31633	0.05413
N1	−0.03827	0.23737	0.01314

the improvement at different sample thicknesses. Unfortunately, these values are extremely difficult to extricate from *CERIUS* in the present version as they have to be derived individually from the *Pendellösung* plots. We show, therefore, only one set of dynamical intensities at a thickness of 100 Å (Table 3). The new *R* factor is 0.30. The value must be considered reasonable for electron diffraction but could probably be improved if a

series of thicknesses were considered and the minimum *R* value found.

A second major problem causing the bad *R* factors is the limited linear range of the photographic emulsion so that the experimental values are not absolutely reliable. In principle, this can be handled by an exposure series. In practice, such a series would be required in each projection, a feat almost impossible to solve with beam-

(a)

(b)

(c)
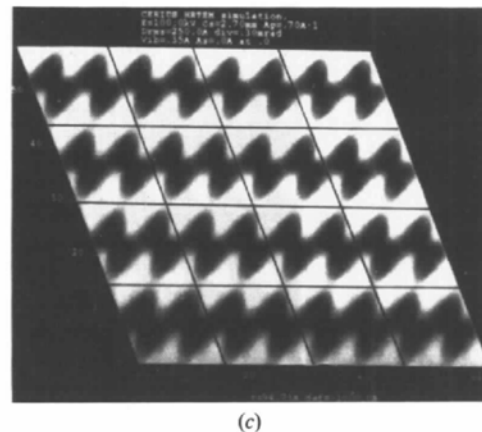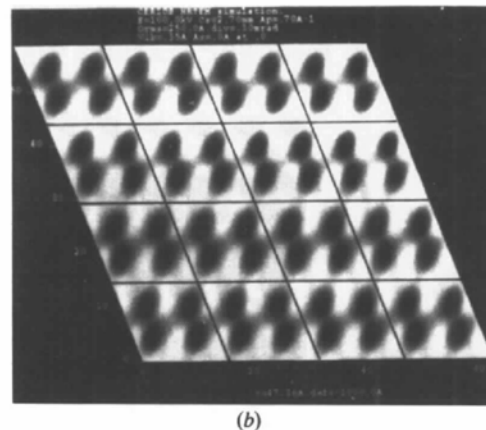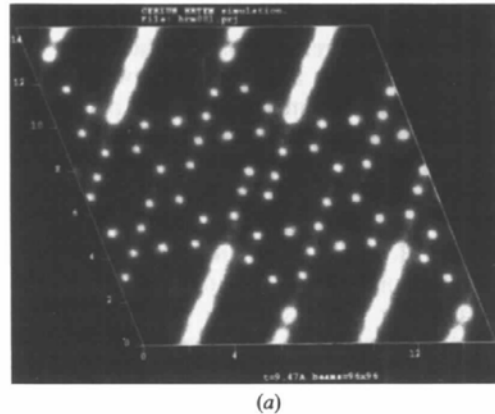
Fig. 9. Simulation of images showing (a) projected potential in *ac* projection with corresponding calculated images for thicknesses of (b) 47 Å and (c) 95 Å.

Fig. 8. *Pendellösung* plot for five representative reflections of CNBA crystal.

sensitive organic samples. Slow-scan CCD cameras will, however, help to alleviate this problem. In view of the extremely low packing energies for the model structures obtained by simulation of the electron diffraction patterns and the good agreement in nine different zones, there is good evidence that the simulated structure is correct. A list of the calculated atomic coordinates is given in Table 4.

4.6. *Simulation of the image*

A convenient representation of the model in the *ac* projection makes a comparison between calculated images, experimental images and the potential maps from maximum-entropy calculation particularly striking. Fig. 9(*a*) shows the *CERIUS*-calculated potential map from the simulated model in Fig. 7(*c*) for a sample thickness of 9.47 Å and defocus 1000 Å. The similarity is apparent. However, with increasing thickness, the image changes markedly. The image for $t = 47$ Å still shows the major features of the potential distribution, but at 95 Å merging of the two adjacent anthryl moieties creates contrast in a new direction with respect to the *b* axis, as observed in the experimental image of Fig. 3. In Figs. 10(*a*), (*b*), (*c*), the effect on the image of increasing the thickness further is shown and compared with the experimental image after *CRISP* processing (Fig. 10*d*).

The relationship between the projected potential and the experimental image is shown to be very complex but still in agreement with the proposed model. It will be seen that the resolution obtained from the maximum-entropy procedure is much better.

4.7. *Ab initio maximum-entropy phasing*

The following procedure was employed:

(1) The 150 unique electron diffraction intensities were normalized to give unitary structure factors, $|U_{\mathbf{h}}|^{obs}$, and their associated standard deviations using the *MITHRIL* computer program (Gilmore, 1984; Gilmore & Brown, 1988) using electron scattering factors and with an imposed overall temperature factor of 5.0 Å.

(2) The remaining calculations used the *MICE* computer program. Three suitable reflections were selected to define the origin and given phase angles of 0°. Image-derived phases were not used here since there are too few to confer any advantage. These reflections thus defined the basis set $\{H\}$.

(3) Node 1 (the root node) of the phasing tree was generated by carrying out a constrained entropy maximization in which the phases and amplitudes of the origin phases were used as constraints to produce a maximum entropy atomic distribution $q^{ME}(\mathbf{x})$.
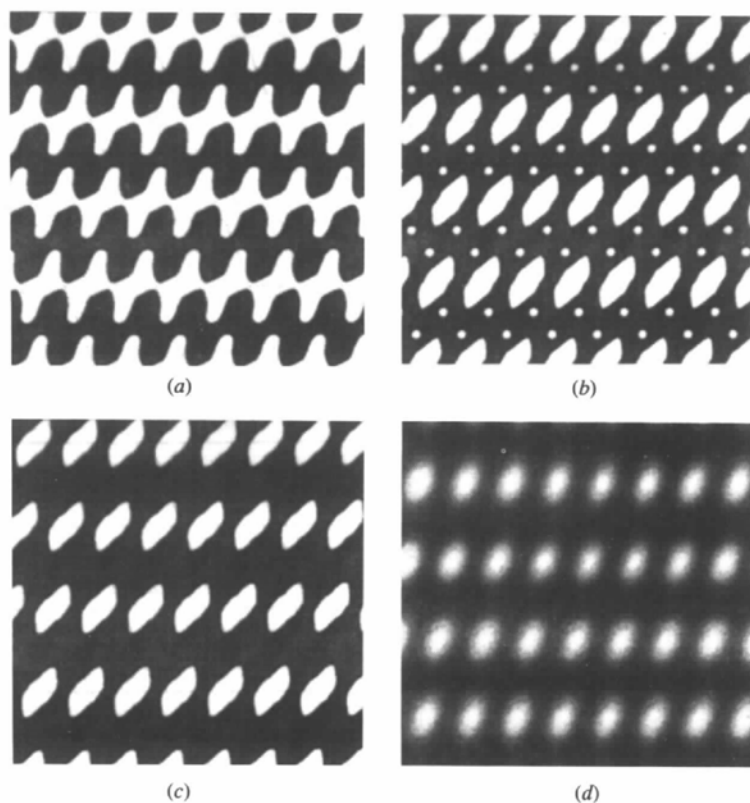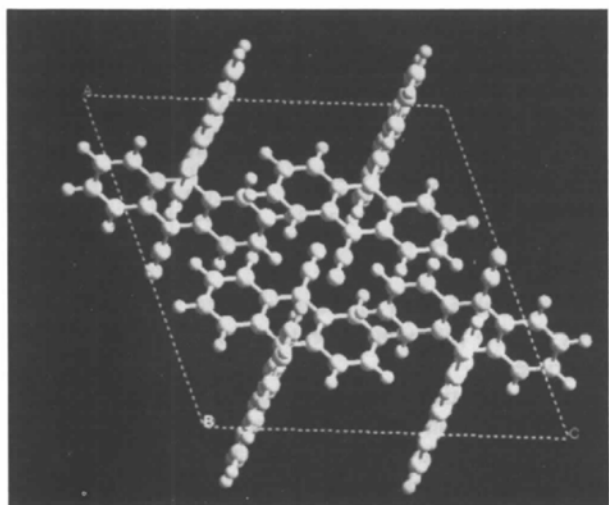

Fig. 10. Comparison between calculated images for sample thicknesses (*a*) 100 Å, (*b*) 150 Å, (*c*) 200 Å. (*d*) Experimental image after processing.
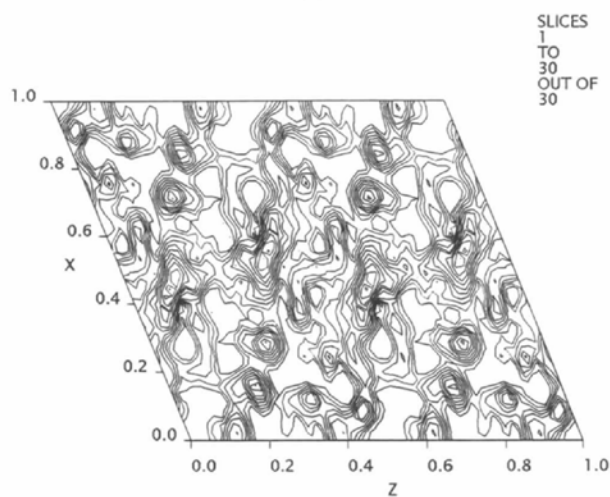
(4) Six strong reflections that optimally enlarged the second neighbourhood of $\{H\}$ were then selected and given permuted phases. Since the space group is centrosymmetric, this generates $2^6 = 64$ nodes which form the second level of the tree (nodes 2–65). Each node was subjected to constrained entropy maximization as in (3) and the LLG computed for each. The Student t test was used to prune this to 16.

(5) The third level of the tree was generated by permuting four more phases, giving $2^4 \times 16 = 256$ new nodes. The entropy maximization and t test was repeated. The solution remaining with the highest LLG was then investigated *via* centroid map generation to give the preferred potential map. This is shown in projection down **b** in Fig. 11(*b*) and in projection down **a** in Fig. 12(*b*). The correspondence with the simulated models in Figs. 11(*a*) and 12(*a*) is apparent.
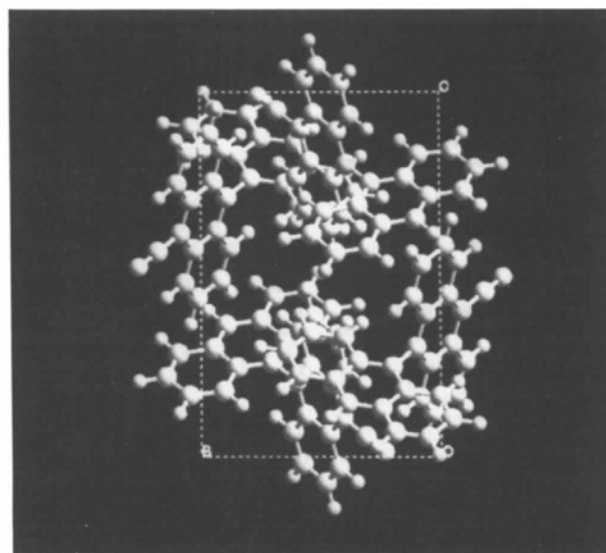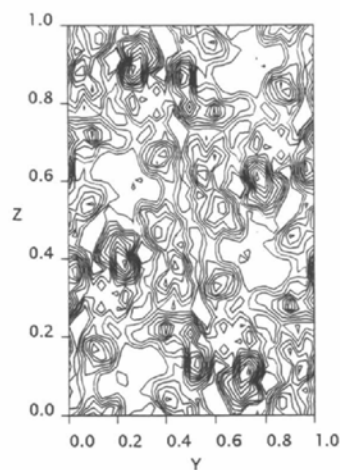
It must be emphasized that the map generated by the ME procedure in no way consulted any imaging data or model-building calculations: it is a model-free procedure.

4.8. *X-ray structural analysis*

The experimental details of the X-ray structure analysis are summarized in Table 5. The final atomic coordinates and equivalent isotropic displacement parameters for the non-H atoms are listed in Table 6. The molecular structure with the crystallographic labelling of the atoms is depicted in Fig. 13(*a*). All of these values appear to be normal and there are no abnormally short intermolecular distances. The two anthracene moieties are planar and twisted through an angle of 84°. The unit cell is monoclinic, with cell constants $a = 14.7021$, $b = 9.4727$, $c = 15.4188$ Å, $\beta = 111.756°$.

(*a*)

(*b*)

Fig. 11. Comparison between structure obtained by (*a*) simulation and (*b*) maximum-entropy-calculated potential map of *ac* projection.

(*a*)

(*b*)

Fig. 12. Comparison between structure obtained by (*a*) simulation and (*b*) maximum-entropy-calculated potential map of *bc* projection.

Table 5. *Experimental details of X-ray scattering*

Crystal data

Chemical formula	$C_{29}H_{17}N$
Chemical formula weight	379.46
Cell setting	Monoclinic
Space group	$P2_1/c$
a (Å)	14.7021 (7)
b (Å)	9.4727 (2)
c (Å)	15.4188 (9)
β (°)	111.765 (4)
V (Å^3)	1994.3 (2)
Z	4
D_x (Mg m^{-3})	1.27
Radiation type	Cu
Wavelength (Å)	1.5418
No. of reflections for cell parameters	75
θ range (°)	65–70
μ (mm^{-1})	0.48
Temperature (K)	298
Crystal form	Prismatic solid
Crystal size (mm)	1.2 × 0.5 × 0.3
Crystal colour	Yellow

Data collection

Diffractometer	CAD-4
Data-collection method	$\omega/2\theta$ scan
No. of measured reflections	7793
No. of independent reflections	3745
No. of observed reflections	3578
Criterion for observed reflections	$F/\sigma(F)>4$
R_{int}	0.06
θ_{max} (°)	70
Range of h, k, l	$0 \to h \to 17$
	$0 \to k \to 11$
	$-18 \to l \to 18$
No. of standard reflections	3
Frequency of standard reflections	4000
Intensity decay (%)	5

Refinement

Refinement on	F
$R[F^2 > 2\sigma(F^2)]$	0.064
$wR(F^2)$	0.064
No. of reflections used in refinement	3578
No. of parameters used	288
Weighting scheme	Unit weights
$(\Delta/\sigma)_{max}$	0.001
$\Delta\rho_{max}$ (e Å^{-3})	0.403
$\Delta\rho_{min}$ (e Å^{-3})	−0.229
Source of atomic scattering factors	*International Tables for X-ray Crystallography* (1974)

Table 6. *Fractional atomic coordinates and equivalent isotropic displacement parameters* (Å^2)

$$U_{eq} = (1/3)\Sigma_i\Sigma_j U_{ij}a_i^* a_j^* \mathbf{a}_i \cdot \mathbf{a}_j.$$

	x	y	z	U_{eq}
C1	0.2932 (2)	0.0973 (3)	−0.0193 (2)	0.061 (1)
C2	0.2216 (2)	0.0003 (3)	−0.0723 (2)	0.066 (1)
C3	0.1606 (2)	−0.0618 (3)	−0.0367 (2)	0.0570 (9)
C4	0.1661 (2)	−0.0297 (2)	0.0563 (1)	0.0435 (8)
C5	0.1030 (2)	−0.0889 (2)	0.0952 (2)	0.0456 (8)
C6	0.1079 (2)	−0.0537 (2)	0.1858 (2)	0.0454 (8)
C7	0.0435 (2)	−0.1128 (3)	0.2259 (2)	0.060 (1)
C8	0.0507 (2)	−0.0757 (4)	0.3132 (2)	0.071 (1)
C9	0.1224 (2)	0.0225 (3)	0.3661 (2)	0.067 (1)
C10	0.1847 (2)	0.0812 (3)	0.3310 (2)	0.0544 (9)
C11	0.1812 (2)	0.0454 (2)	0.2389 (1)	0.0423 (8)
C12	0.2460 (1)	0.1039 (2)	0.2016 (1)	0.0402 (7)
C13	0.2388 (2)	0.0688 (2)	0.1103 (1)	0.0411 (7)
C14	0.3020 (3)	0.1301 (3)	0.0689 (2)	0.0506 (9)
C15	0.2833 (2)	0.6446 (3)	0.2217 (2)	0.084 (2)
C16	0.3699 (2)	0.5932 (3)	0.2830 (2)	0.075 (1)
C17	0.3860 (2)	0.4469 (3)	0.2968 (2)	0.0531 (9)
C18	0.4745 (2)	0.3923 (3)	0.3591 (2)	0.060 (1)
C19	0.4905 (2)	0.2493 (3)	0.3717 (2)	0.0549 (9)
C20	0.5825 (2)	0.1924 (4)	0.4340 (2)	0.075 (1)
C21	0.5972 (2)	0.0533 (4)	0.4448 (2)	0.086 (1)
C22	0.5230 (2)	−0.0437 (4)	0.3956 (2)	0.080 (1)
C23	0.4341 (2)	0.0040 (3)	0.3347 (2)	0.063 (1)
C24	0.4150 (2)	0.1507 (3)	0.3206 (2)	0.0478 (8)
C25	0.3248 (2)	0.2047 (2)	0.2576 (1)	0.0428 (8)
C26	0.3099 (2)	0.3502 (2)	0.2452 (2)	0.0445 (8)
C27	0.2206 (2)	0.4093 (3)	0.1813 (2)	0.0543 (9)
C28	0.2087 (2)	0.5499 (3)	0.1700 (2)	0.072 (1)
C29	0.0306 (2)	−0.1919 (3)	0.0400 (2)	0.0557 (9)
N1	−0.0229 (2)	−0.2737 (3)	−0.0021 (2)	0.0547 (9)

The space group is $P2_1/c$. The orientation of the molecule in the unit cell as determined by X-ray analysis is shown in three projections in Figs. 13(*b*)–(*d*). The structure corresponds therefore to the one obtained by simulation of the electron diffraction pattern with a torsional angle of 83°.

5. Discussion

We have discussed several techniques that demonstrate the power of electron diffraction and high-resolution imaging in order to carry out the structural analysis of a hitherto unknown structure. These include:

(1) Simulation of the experimental diffraction patterns in nine different projections and comparison with experiment.

(2) Simulation and data processing from high-resolution images and comparison with experiment.

(3) *Ab initio* structure determination using maximum entropy and log-likelihood methods. The results are in excellent agreement with one another. Subsequently, a direct-phase X-ray determination was performed and the structure was again substantiated. In view of the fact that many organic materials can only be obtained in the form of microscopically small single crystals or thin films and give rise to only a limited number of reflections, electron crystallography often represents the only means of obtaining vital structural information, so that these new developments will be of considerable benefit to the scientific community.

In many applications, *e.g.* where good mechanical and electro-optical properties in thin films or crystals are required, an analysis of crystal defects is essential. This additional information is provided by the high-resolution images. In this paper, it has been shown how images can be obtained and analysed and which computer software is now available for this purpose. We have described the analysis of defects elsewhere.

In view of the negative packing energy of the crystal and the excellent qualitative agreement between the experimental and simulated diffraction patterns in nine
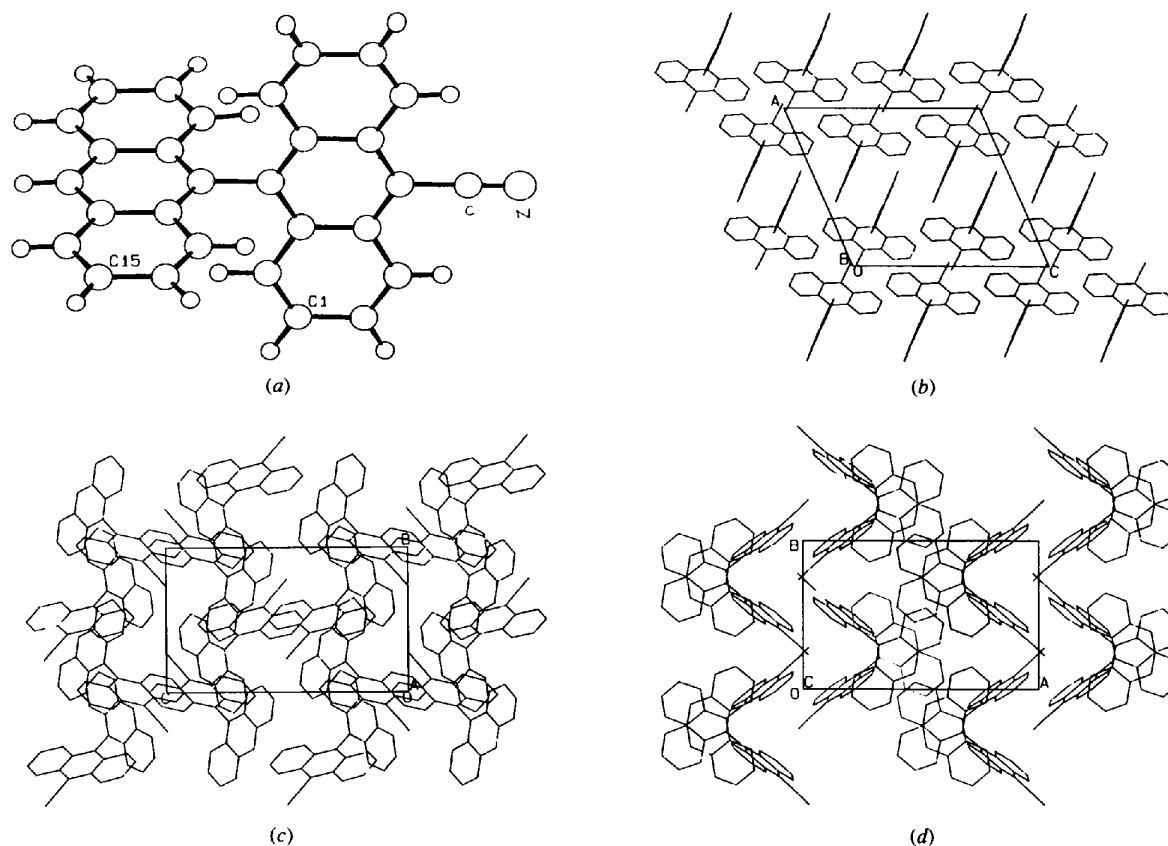
Fig. 13. X-ray structure analysis of 10-cyano-9,9'-bianthryl. (a) Molecule indicating molecular nomenclature in unit cell, (b) in ac projection, (c) in bc projection, (d) in ab projection.

different projections, the disappointing R factors are somewhat surprising. At the same time, we ascertain that the model structure is, in fact, correct, as the X-ray structure analysis indicates. A quantitative estimation of this claim is obtained by calculating an R factor in which the kinematical electron intensities obtained from the simulated model are compared with the X-ray intensities. This value is found to be 0.06, again indicating that the model is correct. In addition, structure determinations based on maximum-entropy statistics gives a potential distribution that also agrees with the model. We have indicated that an improvement of the R factors obtained from experimental electron diffraction can be achieved by increasing the kinematic range (thinner samples, higher voltages), using a recording device with a large dynamic range (slow-scan CCD cameras) and by extending the options to obtain R_{dyn} in *CERIUS*. In fact, it is far more surprising that the correct structure was, in fact, derived, despite the poor R factors. In our view, one explanation lies in the effectiveness of the semi-empirical quantum-mechanical calculations combined with the packing-energy estimations once a structure close to the correct one is qualitatively established on the basis of electron diffraction patterns. The simulation method may also be particularly effective for molecular crystals because there

are so many constraints; frequently, parts of the molecule are very well characterized owing to the nature of their orbitals. Finally, the unit cells of the molecules that we have been investigating are not too large.

References

Amos, L. A., Henderson, R. & Unwin, P. N. T. (1982). *Prog. Biophys. Mol. Biol.* **39**, 183–231.

Bingham, R., Dewar, M. S. & Lo, D. H. (1975). *J. Am. Chem. Soc.* **97**, 1285–1295.

Bricogne, G. (1984). *Acta Cryst.* A40, 410–445.

Bricogne, G. (1988a). *Acta Cryst.* A44, 517–545.

Bricogne, G. (1988b). *Crystallographic Computing 4: Techniques and New Technologies*, edited by N. W. Isaacs & M. R. Taylor, pp. 60–79. Oxford: Clarendon Press.

Bricogne, G. (1991a). *Maximum Entropy in Action*, edited by B. Buck & V. A. Macaulay, pp. 187–216. Oxford Univ. Press.

Bricogne, G. (1991b). *Crystallographic Computing 5: From Chemistry to Biology*, edited by D. Moras, A. D. Podjarny & J. C. Thierry, pp. 257–297. Oxford Univ. Press.

Bricogne, G. (1991c). *Acta Cryst.* A47, 803–829.

Bricogne, G. (1993). *Acta Cryst.* D49, 37–60.

Bricogne, G. & Gilmore, C. J. (1990). *Acta Cryst.* A46, 284–297.

Cowley, J. (1984). *Diffraction Physics.* Amsterdam: North Holland.

Cowley, J. (1988). *Diffraction Physics.* Amsterdam: North Holland.

COWLEY, J. (1992). Editor. *Electron Diffraction Techniqes*, Vol. 1. Oxford Science Publications.

COWLEY, J., REES, A. L. G. & SPINKS, J. A. (1951). *Proc. Phys. Soc.* A64, 609–619.

CRAMER, H. (1946) *Mathematical Methods of Statistics*. Princeton Univ. Press.

CRÉWE, A., ISAACSON, M. S. & ZEITLER, E. (1976). *Advances in Structure Research*, edited by W. HOPPE & R. MASON, Vol. 7, pp. 23–48. Pergamon: New York.

DANIELS, M. E. (1954). *Ann. Math. Stat.* 25, 631–650.

DEWAR, M. S. & YAMAGUCHI, Y. (1978). *Chem. Phys. Lett.* 59, 541–544.

DEWAR, M. S., ZOEBISCH, E., HEALY, E. & STEWART, J. P. (1985). *J. Am. Chem. Soc.* 107, 3902–3909.

DONG, W., BAIRD, T., FRYER, J. R., GILMORE, C. J., MACNICOL, P. D., BRICOGNE, G., SMITH, D. J., O'KEEFE, M. A. & HOVMÖLLER, S. (1992). *Nature (London)*, 355, 605–609.

DORSET, D. (1980). *Acta Cryst.* A36, 592–600.

DORSET, D. (1985a). *J. Electron Microsc.* 2, 89–128.

DORSET, D. (1985b). *Macromolecules*, 19, 2965–2973.

DORSET, D. (1990). *Ultramicroscopy*, 33, 227–236.

DORSET, D. (1991a). *Proc. Natl Acad. Sci. USA*, 88, 5499–5502.

DORSET, D. L. (1991b). *Acta Cryst.* A47, 510–515.

DORSET, D. L. (1991c). *Ultramicroscopy*, 38, 23-40.

DORSET, D. L. (1993). *MSA Bull.* 23, 99–108.

DORSET, D. L. & MCCOURT, M. P. (1994). *Acta Cryst.* A50, 287–292, 344–351.

ELICH, K., LEBIUS, S., WORTMANN, R., PETZKE, F., DETZER, N. & LIPTAY, W. (1993). *J. Phys. Chem.* 97, 9947–9955.

FAN, H., ZHONG, Z., ZHENG, C. & LI, F. (1985). *Acta Cryst.* A41, 163–165.

GILMORE, C. J. (1984). *J. Appl. Cryst.* 17, 42–46.

GILMORE, C. J. & BRICOGNE, G. (1992). Crystallographic Computing 5: *From Chemistry to Biology*, edited by D. MORAS, A. D. PODJARNY & J. C. THIERRY, pp. 298–307. Oxford Univ. Press.

GILMORE, C. J., BRICOGNE, G. & BANNISTER, C. (1990). *Acta Cryst.* A46, 297–308.

GILMORE, C. J. & BROWN, S. R. (1988). *J. Appl. Cryst.* 21, 571–572.

GILMORE, C. J., SHANKLAND, K. & BRICOGNE, G. (1993). *Proc. R. Soc. London*, 442, 97–111.

GILMORE, C. J., SHANKLAND, K. & FRYER, J. R. (1992). *Trans. Am. Crystallogr. Assoc.* 28, 129–139.

GILMORE, C. J., SHANKLAND, K. & FRYER, J. R. (1993). *Ultramicroscopy*, 49, 132–146.

GJØNNES, G. K. & MOODIE, A. F. (1965). *Acta Cryst.* 19, 65–67.

HAN, F., FAN, H. & LI, F. (1986). *Acta Cryst.* A42, 353–356.

HAUPTMAN, H. A. & KARLE, J. (1953). *Solution of the Phase Problem*: 1. *The Centrosymmetric Crystal*. Dayton, OH: Polycrystal Book Service.

HENDERSON, R., BALDWIN, J. M., CESKA, J. A., ZEMLIN, F., BECKMAN, E. & DOWNING, K. (1990). *J. Mol. Biol.* 213, 899–929.

HENDERSON, R. & GLASER, R. (1985). *Ultramicroscopy*, 16, 139–152.

HENDERSON, R. & UNWIN, P. N. T. (1975). *Nature (London)*, 257, 28–32.

HOPPER, W. & HEGERL, R. (1980). *Computer Processing of Electron Microscope Images*. In *Topics in Current Physics*. Berlin: Springer Verlag.

HOVMÖLLER, S. (1992). *Ultramicroscopy*, 41, 121–135.

International Tables for X-ray Crystallography (1994). Vol. IV. Birmingham: Kynoch Press. (Present distributor Kluwer Academic Publishers, Dordrecht.)

KARASAWA, N. & GODDARD, W. A. (1989). *J. Phys. Chem.* 93, 7320–7327.

KLUG, A. (1958). *Acta Cryst.* A46, 515–543.

LIU, Y., FAN, H. & ZHENG, C. (1988). *Acta Cryst.* A44, 61–63.

MAYO, S. L., OLAFSON, B. & GODDARD, W. A. (1990). *J. Phys. Chem.* 94, 8897–8909.

MÜLLER, S. & HEINZE, J. (1991). *Chem. Phys.* 157, 231–241.

POPLE, J. A., BEVERIDGE, D. L. & DABOSH, P. A. (1967). *J. Chem. Phys. Lett.* 47, 2026–2033.

PREDERE, P. (1989). *Ultramicroscopy*, 27, 53–60.

SAXTON, O. (1983). *Ultramicroscopy*, 12, 75–86.

SHANKLAND, K., GILMORE, C. J., BRICOGNE, G. & HASHIZUME, H. (1993). *Acta Cryst.* A49, 493–501.

SHELDRICK, G. M. (1976). *SHELX76*. Program for crystal structure determination. Univ. Cambridge, England.

SHELDRICK, G. M. (1986). *SHELX-86*: Program for the solution of crystal structures. Univ. of Göttingen, Germany.

SIM, G. A. (1959). *Acta Cryst.* 12, 813–815.

STEWART, J. P. (1989). *J. Comput. Chem.* 10, 209–220.

SUBARIC LEIHS, A., MONTE, C., ROGGAM, A., RETTIG, W., ZIMERMANN, P. & HEINZE. J. (1990). *J. Chem. Phys.* 93, 4543–4555.

THIEL, W. & DEWAR, M. J. S. (1977). *J. Am. Chem. Soc.* 99, 4899–4907.

VOIGT-MARTIN, I. G., KRUG, H. & VAN DYCK, D. (1990). *J. Phys. (France)*, 51, 2347–2371.

VOIGT-MARTIN, I. G., SCHUMACHER, M. & GARBELLA, R. (1992). *Macromolecules*, 25, 961-971.

VOIGT-MARTIN, I. G., SCHUMACHER, M. & GARBELLA, R. (1994). *Liquid Cryst.* 17, 775–801.

VOIGT-MARTIN, I. G., SIMON, P., YAN, D. H., YAKIMANSKY, A., BAUR, S. & RINGSDORF, H. (1995). *Macromolecules*, 28, 236–242.

VOIGT-MARTIN, I. G., YAN, D. H., GILMORE, C., SHANKLAND, K. & BRICOGNE, G. (1994). *Ultramicroscopy*, 56, 271–288.

VOIGT-MARTIN, I. G., YAN, D. H., WORTMANN, R. & ELICH, K. (1995). *Ultramicroscopy*, 57, 29–43.

WITTMAN, J. C. & LOTZ, B. (1983). *J. Polym. Sci. (Phys.)*, 21, 2495–2509.

WORTMANN, R., ELICH, K., LEBIUS, S. & LIPTAY, W. (1991). *J. Chem. Phys.* 95, 6371–6381.

WORTMANN, R., ELICH, K., LEBIUS, S., LIPTAY, W., BOROWICZ, P. & GROBOWSKA, A. (1992). *J. Phys. Chem.* 96, 9724–9730.

YAMASAKI, K., ARITA, K. & KAJIMOTO, O. (1986). *Chem. Phys. Lett.* 123, 277–281.

ZOU, X., ZUKHAREV, Y. & HOVMÖLLER, S. (1993). *Ultramicroscopy*, 49, 147–158.